RESEARCH ARTICLE | AUGUST 20 2024

Identification of no-fly zones for delivery drone path planning in various urban wind environments

Special Collection: Flow and Civil Structures

Shan Jiang (姜山) ; Jinghan Wang (王靖含) ; Chao Li (李朝) ; Jinping Ou (欧进萍); Penghao Duan (段鹏浩) ; Lishuai Li (李立帅)

Physics of Fluids 36, 085166 (2024)
https://doi.org/10.1063/5.0221281

Physics of Fluids ARTICLE pubs.aip.org/aip/pof

Identification of no-fly zones for delivery drone path planning in various urban wind environments

Cite as: Phys. Fluids **36**, 085166 (2024); doi: 10.1063/5.0221281
Submitted: 31 May 2024 · Accepted: 29 July 2024 ·
Published Online: 20 August 2024

Shan Jiang (姜山),[1,a)] Jinghan Wang (王靖含),[1,2,b)] Chao Li (李朝),[2,3] Jinping Ou (欧进萍),[2,3] Penghao Duan (段鹏浩),[1,b)] and Lishuai Li (李立帅)[1,4,5]

AFFILIATIONS

[1]Department of Mechanical Engineering, City University of Hong Kong, Hong Kong SAR, China
[2]Harbin Institute of Technology, Shenzhen, Shenzhen, China
[3]Guangdong Provincial Key Laboratory of Intelligent and Resilient Structures for Civil Engineering, Harbin Institute of Technology, Shenzhen, China
[4]School of Data Science, City University of Hong Kong, Hong Kong SAR, China
[5]Hong Kong Institute for Data Science, City University of Hong Kong, Hong Kong SAR, China

Note: This paper is part of the special topic, Flow and Civil Structures.
[a)]**Electronic mail:** sjiang75-c@my.cityu.edu.hk
[b)]**Authors to whom correspondence should be addressed:** wjh900607@163.com and pengduan@cityu.edu.hk

ABSTRACT

A drone delivery system, characterized by its low energy consumption, high efficiency, and extensive coverage capability, has been adopted as an effective solution to overcome the limitations of traditional ground transportation. However, due to strong interactions between urban structures and wind, the wind environment in the low-altitude airspace of urban areas poses significant safety risks for drone operations, a challenge that remains unresolved. To mitigate these risks, this study presents a methodology for precisely defining the no-fly zones (NFZs) for drone operations using computational fluid dynamics (CFD) simulations. Three hazardous indices—safe, deviation, and unsafe—are proposed to indicate the drone operation status. High-resolution CFD models of urban wind environments in a real city area are coupled with meteorological wind data to provide statistical results for the three indices. The Reynolds-averaged Navier–Stokes turbulence model is employed to simulate two wind environments, standard wind and strong wind, under 36 incoming flow directions. Considering eight flight orientations of drone operating in horizontal planes at various heights, a set of maps for the occurrence probability of the three hazardous indices is provided. These maps can be utilized to determine safe areas, identify no-fly zones corresponding to high occurrence probabilities of deviation and unsafe indices, and establish efficient flight paths for drone operations.

I. INTRODUCTION

The growth of e-commerce has led to an increase in online purchases. As a result, the logistics industry faces more stringent timeliness requirements due to the growing number of consumers. Simultaneously, the ongoing growth of e-commerce has significantly impacted the environment, particularly in the final delivery of goods. This impact is primarily due to inefficient truck loading, increased delivery frequency, and poorly planned distribution routes.[1] The development of new logistics solutions and the use of low-fuel-emission means of transportation have been driven by increased customer demand and the need to protect the environment.[2] Combined with drones, an air-ground integrated logistics and distribution network is a viable solution compared to traditional ground-based distribution methods. According to Kirschstein,[3] technological advances in drones are transforming the last mile of delivery, bringing cost reductions while increasing user satisfaction with timeliness. The assessment of emissions and efficiency for last-mile delivery by drones vs trucks shows the overall performance of drones is economically feasible.[4] Companies like Amazon and DHL have explored the possibilities of drones in the logistics sector, notably their ability to overcome terrain constraints and complex building environments.[4,5]

To improve the efficiency of drone logistics and ensure the flight safety of drones in urban areas, it is essential to plan drone flight paths considering the complexity of the surrounding environment in low-

altitude airspace. The urban wind environment (UWE), characterized by the wind field in a city influenced by buildings, topography, and artificial structures, shows significant impacts on drones' flight. Although the UWE typically exhibits lower average wind speeds compared to the wind environment of rural areas, local wind speeds can be significantly higher at specific locations near buildings and structures.[6] In addition, the urban wind fields are quite complex due to the changes in the wind direction and local wind turbulence, which is affected by varying heights and densities of urban buildings, rendering the wind field more unstable and unpredictable.[7,8] This complex UWE poses substantial challenges to the safety and stability of drone flights. During operations, drones encounter aerodynamic drags and wind gusts caused by the surrounding wind environment.[9] Research into the various wind effects on drones has highlighted that factors such as constant wind, turbulent flow, wind shear, and propeller vortex mainly alter the airspeed of drones.[10] Variations in airspeed affect the angle of attack and side-slip angle, resulting in disturbance to the resultant force and torque. These wind-induced disturbances lead to additional energy consumption and increased complexity in path planning and urban air mobility management.[11]

The UWE can be investigated using field measurements, scaled-down physical wind tunnel tests, and numerical simulations, or a combination of these methods. On-site measurements are the most effective way to study unmanned aerial vehicle (UAV) flight in UWE, as they provide a realistic representation of the effects of wind flow fields on drones. However, the complexity and variability of UWE can lead to uncontrollable measurement results when using the standard point measurement method. Uncontrolled measurement UAVs due to unreasonable wind loads can pose safety hazards to nearby buildings and pedestrians. In addition, two aspects restrict the application of physical wind tunnel tests in evaluating UWE. First, point measurements are limited in capturing detailed flow structures. Second, meeting the pivotal similarity parameters governing specific flow patterns, including Reynolds number, geometric similarities, turbulence intensity and length scale, and surface roughness,[12,13] can be challenging or expensive. Therefore, due to the rapid advancement of computer platforms, computational fluid dynamic (CFD) techniques have become the primary research method for simulating the UWE.[14] Numerical simulation of UWE using CFD is a valuable alternative due to its detailed representation of the flow field across the entire computational domain, as well as its cost and time efficiency. By selecting an appropriate solver, such as the Reynolds-Averaged Navier–Stokes (RANS), the unsteady RANS (URANS), and the large eddy simulation (LES),[14–16] the desired physical parameters of the wind flow field in the full-size or scaled computational domain can be obtained. Previous research has demonstrated that CFD methods can provide results that meet accuracy requirements and engineering application needs for the pedestrian wind environment,[17–19] wind energy consumption,[6,20,21] pollutant dispersion in urban areas,[22] and architectural design.[23,24]

In the context of the aforementioned research, several studies have employed CFD to simulated the urban wind environment and determine appropriate flight areas or paths for drones in the cities. Orr *et al.*[25] developed a UAV control algorithm that incorporates CFD results to evaluate the flight behavior of a small UAV in a real urban scenario, providing different flight paths for windless and windy conditions. Galway *et al.*[26] used CFD to create a database of building wake turbulence for wind conditions and typical building configurations in North American urban areas. Their selection algorithm determines if building wake affects an aircraft's current position and identifies where flight is most affected within a given wake flow. Ware and Roy[27] investigated the ability of a quadrotor to exploit wind fields to improve its flight performance, using an empirically derived power consumption model and wind field estimation to find the minimum energy-consumption trajectory. Paz *et al.*[28] evaluated the impact of proximity to walls on drone performance using CFD and dynamic mesh-based methods for delivery drones that typically fly near building walls, finding that additional pitching moment variations need to be counteracted when approaching and leaving obstacles to ensure the stability and safety. Jeong *et al.*[29] applied CFD simulation combined with a deep neural network to model the wind environment and provide information for operation risk management and path planning, indicating hazardous flight areas based on the deviation from the original flight path caused by the wind environment. However, the studies mentioned above either use simplified urban models or smaller-scale models of the city, such as cubes to represent building complexes, which can result in an incomplete portrayal of the drone airworthiness area due to deviations from the natural environment.

Based on the research background, methodology, and areas for improvement identified in the existing studies, this study aims to precisely simulate the wind field distribution in the low-altitude airspace of a large-scale urban area using RANS. The primary objective is to delineate the flight exclusion zones that directly impact the safe and stable operation of delivery drones within the urban environment. Additionally, this research provides valuable insights for drone path recognition and planning, while inspiring the development of comprehensive urban wind environment databases. The remainder of the study is arranged as follows: Sec. II describes the city and CFD models used for simulating the UWE. Section III presents the analysis and discussion of the UWE result, including the wind field, recognition criteria of the no-fly zone (NFZ), and flight hazardous maps. The conclusion of the study is summarized in Sec. IV.

II. MODEL SETUP

A. Urban environment and wind data

Mong Kok district is located in the central part of the Kowloon Peninsula in the Hong Kong Special Administrative Region. Surrounded by the districts of Sham Shui Po, Tai Kok Tsui, and Yau Ma Tei, it is one of the busiest commercial districts in Hong Kong. Characterized by dense clusters of stores, high-rise office and residential buildings, and a complex transportation network,[30] this area faces high demands for logistics. However, the efficiency of the traditional ground transportation system is often hindered by traffic congestion caused by narrow streets. In response, establishing a flight route network for delivery drones appears promising to meet the high logistics demands. It is essential to consider the building environment in the low-altitude airspace and the weather conditions, specifically the wind environment that poses a safety risk to drone flights, during the route planning stage to balance the safety and efficiency of the drone transportation system. Therefore, as shown in Fig. 1(a), this study selects a circular area with a radius of 1250 m as the object Urban Area (UA) that covers all of Mong Kok and some neighboring areas.

Additionally, since there is an automatic weather station within the objective UA, the King's Park (KP), wind data recorded from 2014 to 2023 was obtained from the Hong Kong Observatory website.[31,32]

to accurately represent the wind conditions in this region. The corresponding wind rose diagram is shown in Fig. 1(b). The meteorological observations reveal a prevailing wind direction predominantly from the east to southeast throughout the year, with the highest probability of occurrence at a bearing of 100°. Moreover, the annual average wind speed is 2.5 m/s, with this speed showing the greatest probability of occurrence. Conversely, other wind directions exhibit lower probabilities of occurrence and correspondingly lower average wind speeds.

B. Numerical strategies

1. SST $k-\omega$ turbulence model

In this study, the effects of the prevailing mean wind flow on drone operations are primarily investigated. Therefore, the incompressible steady-state Reynolds-averaged Navier–Stokes (RANS) turbulence model is utilized to conduct all CFD simulations. Given its capability and robustness of predicting wall-bounded flows and separation behind buildings,[16,33] the two-equation $k-\omega$ shear stress transport (SST) model[34,35] is selected. As known, the governing equations for an incompressible flow without external forces are given in the following equations:

$$\frac{\partial \overline{u_i}}{\partial x_i} = 0, \tag{1}$$

$$\frac{\partial \overline{u_i}}{\partial t} + \overline{u_j}\frac{\partial \overline{u_i}}{\partial x_j} = -\frac{1}{\rho}\frac{\partial p}{\partial x_i} + \frac{\partial}{\partial x_j}(2\nu_t S_{ij} - \overline{u_i' u_j'}), \tag{2}$$

$$S_{ij} = \frac{1}{2}\left(\frac{\partial \overline{u_i}}{\partial x_j} + \frac{\partial \overline{u_j}}{\partial x_i}\right), \tag{3}$$

$$\nu_t = \frac{a_1 k}{\max(a_1\omega, b_1 F_2 S_{ij})}, \tag{4}$$

$$F_2 = \tanh\left[\left[\max\left(\frac{2\sqrt{k}}{\beta^*\omega y}, \frac{500\nu}{y^2\omega}\right)\right]^2\right], \tag{5}$$

where $\overline{u_i}$ and p are the mean of velocity and pressure, respectively. ν_t is the turbulent viscosity. S_{ij} is the mean strain rate tensor. k is the turbulent kinetic energy (TKE). $\overline{u_i' u_j'}$ is the Reynolds stress term computed by the $k-\omega$ turbulence model. $a_1 = 0.09$, $b_1 = 1.0$, and $\beta^* = 0.09$ are the model constants. y is the distance to the nearest wall. ν is kinematic viscosity. ω is the turbulence specific dissipation rate.

The RANS simulation is conducted using OpenFOAM-v2306. A semi-implicit method for pressure-linked equation (SIMPLE) algorithm[36] is adopted to solve the pressure-velocity coupling problem. Numerical schemes take the implemented schemes in OpenFOAM. The time scheme is steadyState. The gradient terms are discretized using the cellLimited Gauss linear method with a limiting coefficient of 1.0. The divergence schemes are set as Gauss LUST unlimitedGrad (U) for (ϕ, U), Gauss limitedLiner 1 for (ϕ, k) and (ϕ, ω), respectively. A Gauss linear uncorrected scheme is used for Laplacian terms related to ω. The convergence criteria are set as 1×10^{-6} for momentum and scalar transport equations.

2. Computational domain and boundary conditions

As illustrated in Fig. 2(a), a prototype computational model is established, which stretches 6000 m in the longitudinal direction, 4500 m in the transverse direction, and 1000 m in the vertical direction, following the recommendation of the Architectural Institute of Japan (AIJ) guideline proposed by Tominaga *et al.*[37] This guideline recommends a minimum distance of 5H from the inlet and top boundary to the target city and a minimum distance of 10H from the outlet to the city, where H is the height of the building of concern. In this study, the focus is not on a single building but on the area around

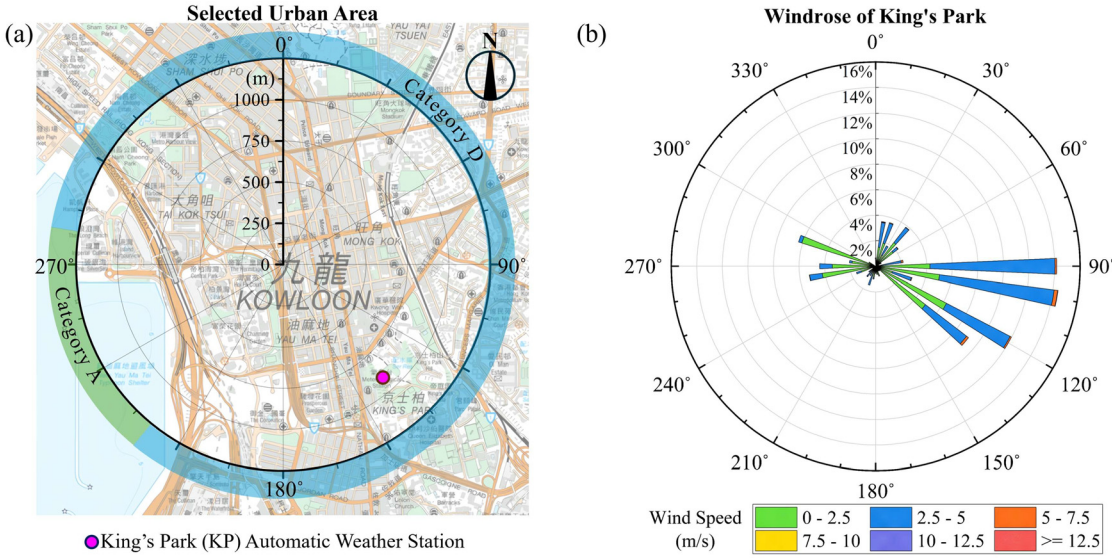

FIG. 1. Field and wind information of the objective urban area with (a) city range and surrounding terrain category, and (b) windrose map at the KP weather station.

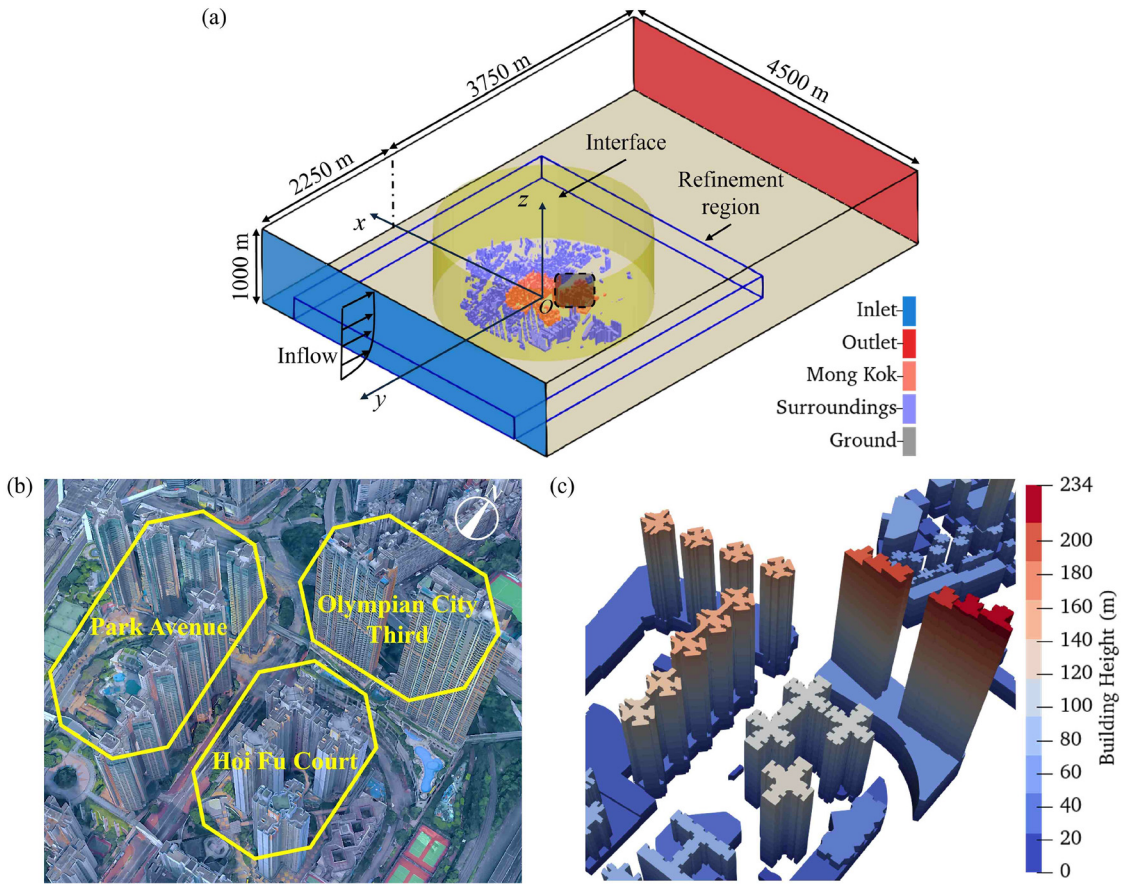

FIG. 2. (a) Computational domain, boundary faces, selected area (grey shaded) in Mong Kok, (b) the real buildings in the selected area, and (c) model representation of real buildings.

the building, thus H is set as 200 m considering that the tallest building in the selected UA equals 234 m, and the average height of less than 200 m. In addition, the blue outlined box in Fig. 2(a) denotes the mesh refinement region (length: 4000 m, width: 3500 m, height: 300 m). The 1250 m diameter cylindrical surface is the interface between UA and the surrounding outer region (SOR). Using the intersection interface facilitates the subsequent ability to simulate different wind directions by rotating SOR. The grey-shaded area is extracted to show the high-resolution geometry representing the real buildings of the selected area in Mong Kok, as shown in Figs. 2(b) and 2(c).

Following the power-law inflow condition described by Yang *et al.*,[33] the mean velocity $U(z)$, k, and ω are specified at the Inlet boundary. The corresponding profiles are given in the following equations:

$$U(z) = U_{\text{ref}}\left(\frac{z}{z_{\text{ref}}}\right)^{\alpha}, \tag{6}$$

$$k = \frac{3}{2}(U(z)I(z))^2, \tag{7}$$

$$\omega(z) = \frac{\alpha}{\sqrt{C_\mu}}\frac{U(z)}{z}, \tag{8}$$

where U_{ref} is the reference velocity at a specific altitude, z_{ref} is the reference altitude, and α is the power law exponent determined by the terrain category. $I(z)$ is the turbulent intensity, determined according to AIJ Recommendations for Loads on Buildings,[38]

$$I(z) = \begin{cases} 0.1\left(\dfrac{z}{z_G}\right)^{-\alpha-0.05}, & z \le z_G, \\ 0.1, & z > z_G, \end{cases} \tag{9}$$

where z_G is the boundary layer height related to the terrain category. C_μ is an empirical constant of the turbulence model and equals 0.09. The parameters corresponding to the inflow conditions, namely α and z_G, are determined based on building heights and densities within the surrounding region of the study area. According to the Chinese Code for Structural Load Design of Buildings (GB 50009-2012), Category A terrain includes offshore sea and islands, coasts, lakeshores, and desert areas, while category D terrains refers to urban areas with dense building clusters and taller structures. The surrounding terrain is thus

classified into two categories: Category A for wind directions within range of 220°–280° and Category D for the remaining wind directions. The corresponding parameters are $\alpha = 0.12$ and $z_G = 300\,\text{m}$ for Category A, and $\alpha = 0.30$ and $z_G = 550\,\text{m}$ for D.

Furthermore, regarding the other boundaries shown in Fig. 2(a), a cyclicAMI boundary condition is applied at the interface pair boundary that connects the UA and SOR. A no-slip wall condition is used at the Mong Kok, Surroundings, and ground boundaries. A zero-gradient condition is applied at the Outlet boundary, and a symmetry condition is applied at the remaining domain side boundaries.

3. Mesh schemes and grid-independence study

Two built meshing tools in OpenFOAM, snappyHexMesh, and cfMesh were employed for grid generation for the UA and SOR. The tools utilize octree algorithms to generate high-quality Cartesian grids capable of capturing complex geometric shapes. Both methods determine the minimum grid size within a given geometry surface or region by defining the background grid size and optimizing it based on the background grid size. The size relationship can be expressed using the following formula:

$$\Delta x = \frac{X_0}{2^n}, \tag{10}$$

where Δx is the mesh size for a given surface or region, X_0 is the background mesh size, and n is the refinement level.

Following the AIJ guideline[37] and the ten tips for reliable CFD simulations,[14] X_0 is 50 m in this study. The remaining mesh parameters are listed in Table I. Utilizing this setup, the minimum grid size is 0.78 m for Mong Kok and 1.5 m for the surroundings, corresponding to the minimum resolution proposed in AIJ guidelines (about 0.5–5.0 m near the target building if evaluation is performed in the adjacent area).[37] The Cartesian mesh generated guarantees a sufficient overall grid resolution and mesh quality (skewness, orientation, and aspect ratio). Figure 3 shows the mesh details of domain inlet, refinement region, ground boundary layer (BL), interface boundary, domain symmetry, and domain ground along with the area selected from surroundings and Mong Kok.

As listed in Table I, two computational meshes, baseline and refined, are employed in this study to implement the grid-independence study. The main difference between these two meshes is the different grid sizes within the refinement region, as shown in Fig. 2(a). Finally, the baseline mesh contains 53.59×10^6 cells with 85% hexahedra cells and 15% prisms and polyhedral cells. The refined mesh comprises 78.31×10^6 cells, around 1.5 times the baseline mesh.

TABLE I. Mesh parameters for the two computational models.

Surface/Region	Refinement level (n)	Minimum grid size	Maximum grid size
Mong Kok	(5, 6)	0.78 m	1.56 m
Surroundings	(4, 5)	1.56 m	3.12 m
Inlet/Outlet /Symmetry	0	···	50 m
Ground /Refinement region	2 for baseline mesh	···	12.5 m
	3 for refined mesh	···	6.25 m

Two case studies were conducted using a WE1 setup and a wind direction of 100° on the baseline and the refined mesh. Mesh details for the Mong Kok (MK) region are provided in Fig. 4(a) for baseline mesh and Fig. 4(b) for refined mesh. The mesh setup for the building surface remains unchanged in both cases to ensure compliance with AIJ requirements. The refinement region is modified to determine whether the grid resolution is sufficient to capture the flow details in the areas away from the buildings where the drone operations take place.

Two locations at KP and MK, as shown in Fig. 5(a), are selected for extracting velocity profile along the vertical direction. The comparison of the mean velocity distributions at the KP and MK positions is given in Figs. 5(b) and 5(c), respectively. Results show the mean velocity obtained using the baseline mesh is in close agreement with those obtained using the refined mesh. In addition, the mean absolute value of the relative error (MARE) of the mean velocity between the two mesh schemes is 0.75% for the KP position and 8.8% for the MK position, as shown in Fig. 6. This indicates that refining the mesh on top of the baseline mesh has a minimal impact on the results, and the baseline mesh is sufficiently fine for subsequent simulations.

III. RESULTS AND DISCUSSION

Following the aforementioned CFD setup and utilizing the baseline mesh, two types of wind environments (WEs) within the Mong Kok region are modeled. WE1 adopts the recorded wind data at the KP weather station and represents the normal drone operation condition. Moreover, an extreme condition, WE2, is defined using a reference wind speed of 12 m/s at a height of 120 m, which corresponds to level six on the Beaufort Wind Scale and indicates a strong wind condition. Detailed parameters defining the CFD cases are provided in Table II.

A. Wind distribution in low-altitude airspace

To demonstrate the UWE within the low-altitude airspace of the Mong kok region and its impact on drone flights in detail, two sample routes (SRs) for drone operation, SR1 and SR2, varying from 100 to 115 m, are selected and shown in Fig. 7. In this section, the drone navigates SR1 from A to B and SR2 from C to D. These routes are proposed to achieve optimum efficiency by considering the shortest distance between each pair of origin-destination (OD) without accounting for wind effect.[39]

Figure 8 shows the wind velocity distribution under WE1 and WE2 at a height of 100 m within Mong Kok region, including SR1 and SR2. The surface line integral convolution (LIC) method is adopted to illustrate the flow streamlines of the local wind. According to the contours, it is obvious that both SR1 and SR2 pass through areas with varying wind speeds and directions. In addition, under the same inflow direction, local wind speeds in front of the buildings and in open areas are influenced by the inflow wind speeds, exhibiting stable flow patterns and an increase in wind speeds corresponding to higher incoming wind speeds. However, in the leeward region of buildings, local wind speeds are significantly affected by flow separation around the structures. Moreover, the incoming wind direction substantially impacts on the local wind distribution in the selected region due to the diverse building environments around the two SRs. For instance, most parts of SR1 are located in the windward region of the buildings under

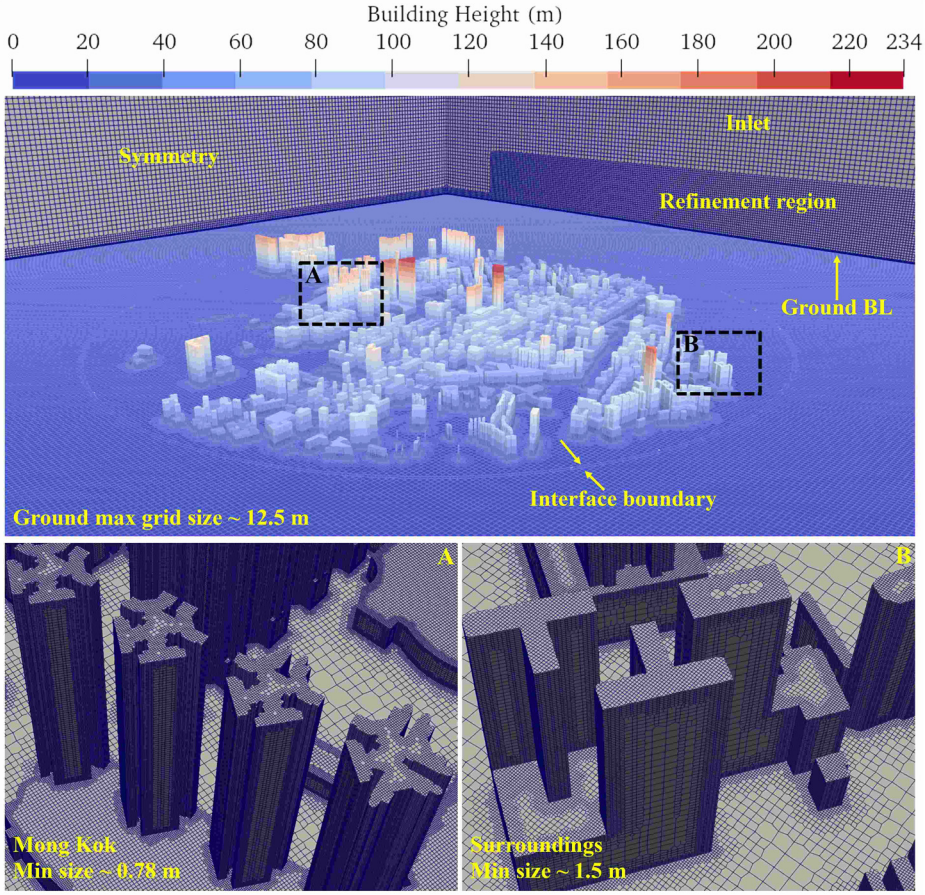

FIG. 3. Surface mesh details of computational domain with extraction area (a) showing region from Mong Kok, extraction area (b) showing region from surroundings.

a 0° inflow wind direction of but shift to the leeward region under a 100° inflow wind. This phenomenon is quantitatively described in Fig. 9, which shows the wind speed distribution along the specified flight routes.

Figure 9 shows that the wind velocity distribution along the two SRs varies significantly under specific incoming flow conditions, potentially preventing drones from operating in a safe wind environment. Changes in incoming wind direction can cause large variation in local velocity magnitudes at the same point. For instance, at the point close to the destination in SR1 (point B) and near point D in SR2, the wind speed peaks with an incoming wind direction of 0° but decreases when the incoming wind direction shifts to 100°. This indicates that a

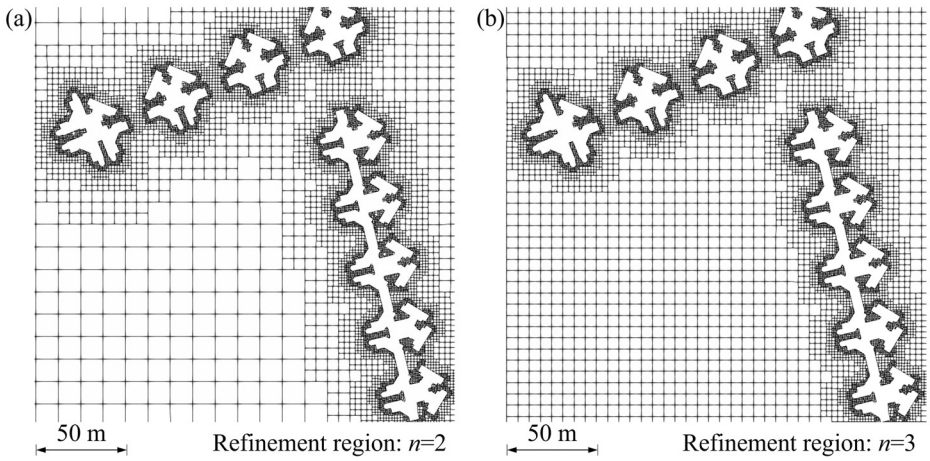

FIG. 4. Mesh details in the MK region of (a) baseline mesh and (b) refined mesh.

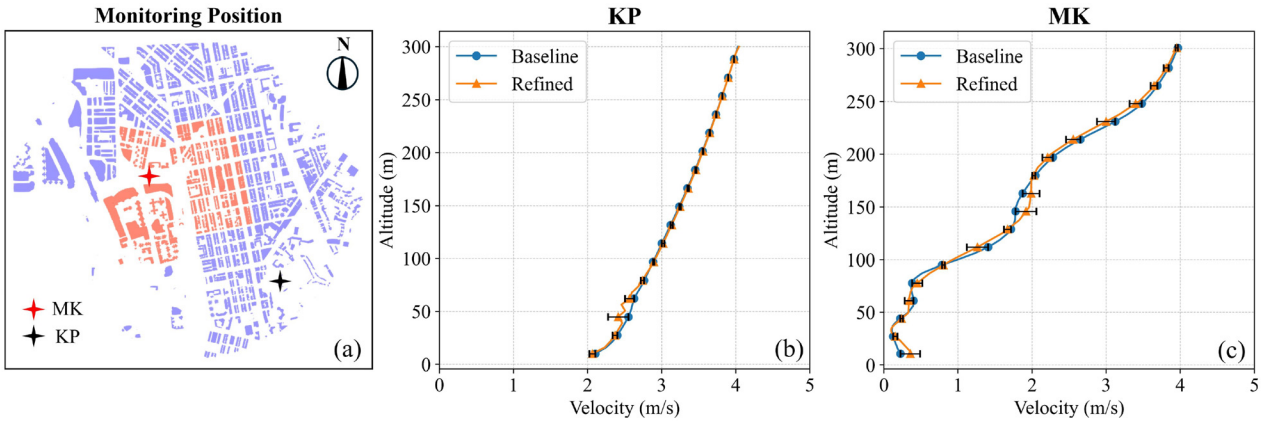

FIG. 5. Data extraction for mesh independent study with (a) showing the monitoring position, (b) the velocity profile at KP, and (c) the velocity profile at MK.

location safe for drone operation in one wind direction can become hazardous if the wind direction changes.

B. Definition of no-fly zones

At present, the pre-defined no-fly zone is set at 10–30 m from the buildings, as specified by the Safety Requirements Document for Small Unmanned Aircraft Operations by the Civil Aviation Department of The Government of the Hong Kong Special Administrative Region.[40]

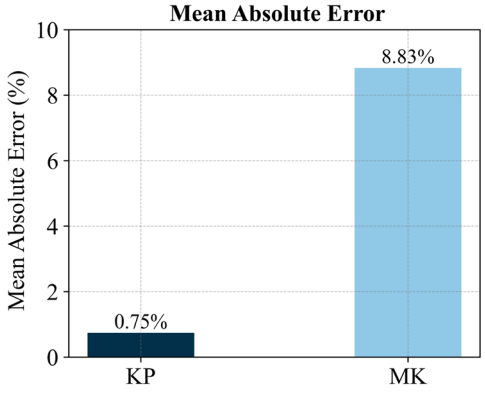

FIG. 6. Mean absolute value of relative error of velocity obtained using two meshes at two locations.

However, this definition does not account for wind effects in low-altitude airspace of urban areas and may overestimate the range of no-fly zone. The safety of drone operations outside this pre-defined zone remains uncertain. Therefore, this study uses a stepwise approach to define no-fly zones, aiming to more fully consider more fully the impact of buildings and the urban wind environment. The first step defines the UAV flight hazardous indices, the second step determines the hazard level based on the these indices, and the final step establishes the no-fly zone based on the hazard level.

Step 1: defining the flight hazardous indices. As illustrated in Fig. 10, three scenarios can be encountered by a drone when it navigating an established flight route. Following the aforementioned stepwise approach, the hazardous index and flight scenario correspond as follows:

(1) Safe: the drone navigates its programed flight route, with the magnitude of $\boldsymbol{u}_w$ and $\boldsymbol{u}_r$ not exceeding $\hat{u}$,
(2) Deviation: the magnitude of $\boldsymbol{u}_r$ is above $\hat{u}$, and $\boldsymbol{u}_r$ is not parallel with $\boldsymbol{u}_d$,
(3) Unsafe: the magnitude of $\boldsymbol{u}_w$ exceeds $\hat{u}$, where $\boldsymbol{u}_d$, $\boldsymbol{u}_w$, and $\boldsymbol{u}_r$ are all velocity vectors in 3D space, with $\boldsymbol{u}_d$ representing the ground speed of the drone, $\boldsymbol{u}_w$ denoting the regional wind velocity acting on the drone, and $\boldsymbol{u}_r$ referring to the resultant velocity of those two velocities. The angle between the wind velocity $\boldsymbol{u}_r$ and the drone's flight speed $\boldsymbol{u}_d$ is ψ. $\hat{u}$ is the upper velocity threshold for safe operation. In this study, $\hat{u}$ is set as 10 m/s. The value is determined by considering: the maximum wind resistance of typical delivery drones listed in

TABLE II. Parameters defining the CFD cases.

WE	U_{ref} (m/s)	z_{ref} (m)	Terrain category	α	z_G (m)	Wind angle (10° interval)
WE1	2.5	65	A	0.12	300	220°–280°
			D	0.3035	550	0°–210°, 290°–310°, 330°–350°[a]
WE2	12	120	A	0.12	300	220°–280°
			D	0.3035	550	0°–210°, 290°–350°[b]

[a]Exclude 320° for the number of occurrences is zero based on the 10-year measurement.
[b]Include 320° to provide a complete picture of the impact of possible extreme wind speeds.

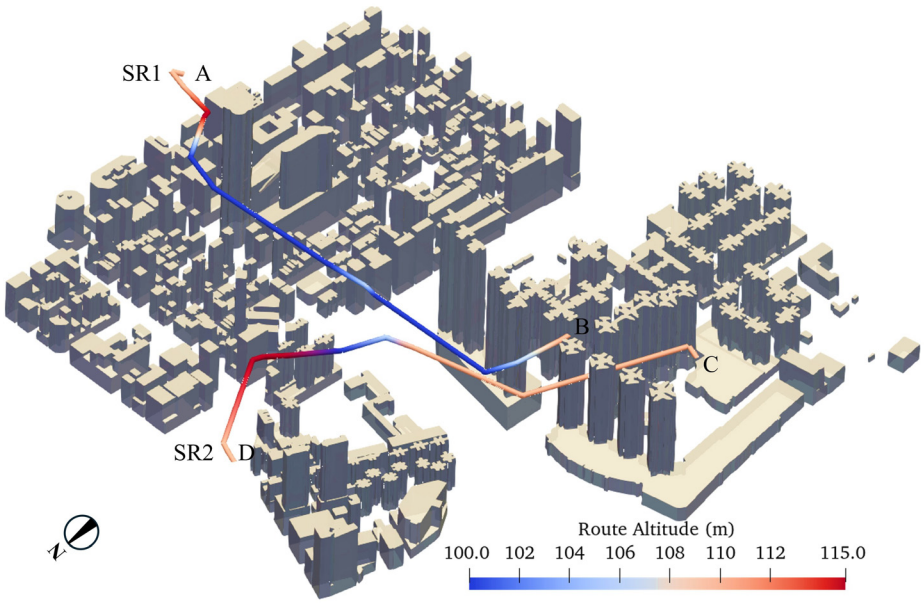

FIG. 7. Two sample routes for drone operation at Mong Kok.

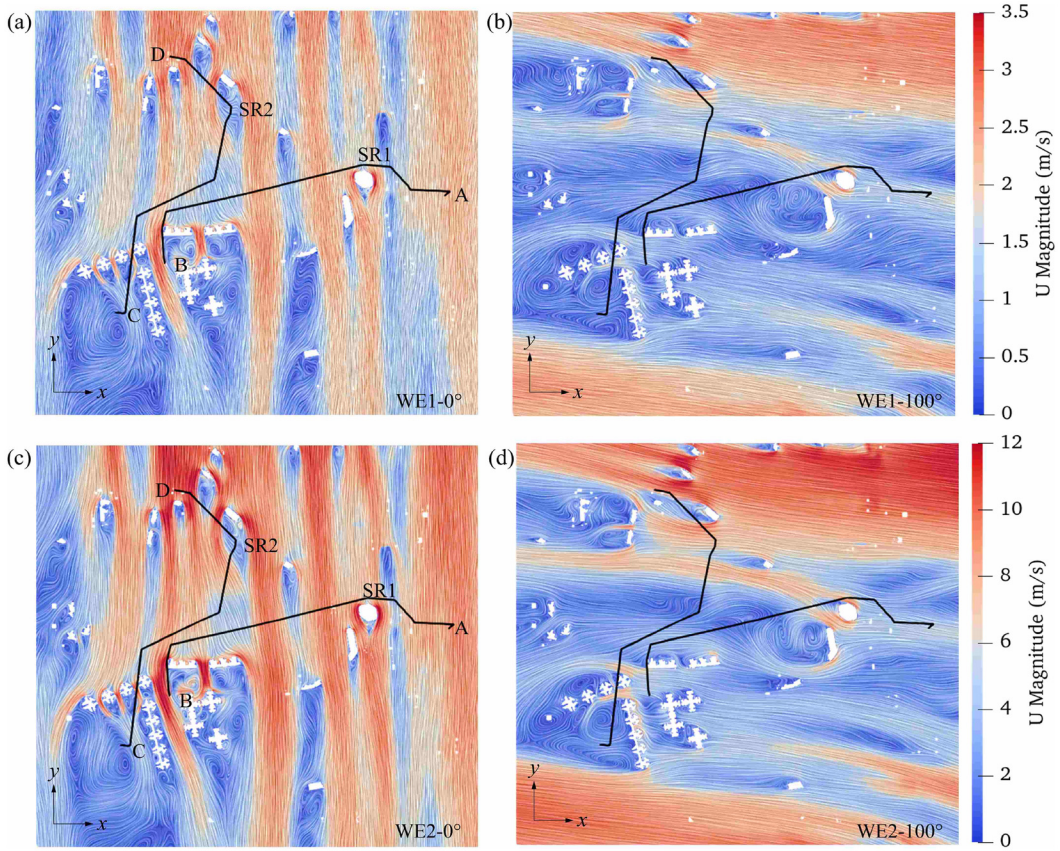

FIG. 8. Contours of wind velocity at 100 m altitude under different wind environments and directions with (a) WE1-0°, (b) WE1-100°, (c) WE2-0°, and (d) WE2-100°.

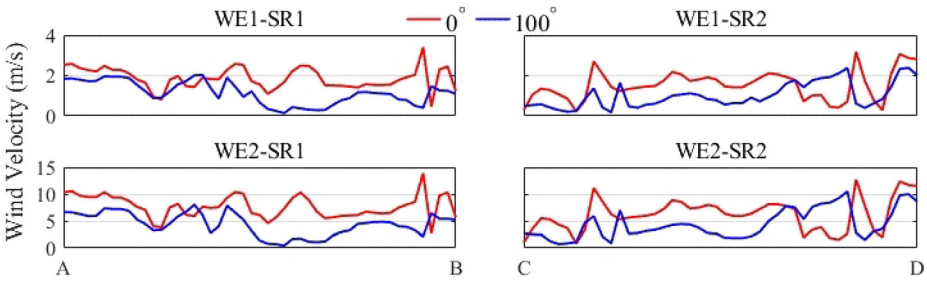

FIG. 9. Comparison of wind speeds along SR1 and SR2 under WE1 and WE2 with an inflow direction of 0° and 100°.

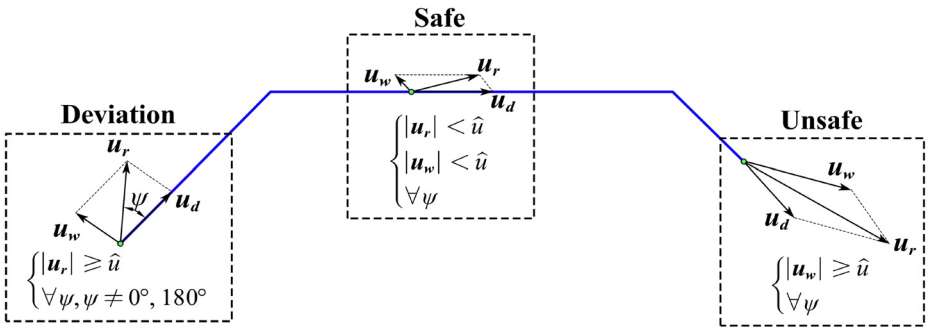

FIG. 10. Three scenarios along the flight route (blue line) and the drone operation hazardous index definition.

Table III and a safety factor of 1.2. The safety factor, maximum wind resistance, and $\hat{u}$ are related by

$$Safety\ factor = \frac{Maximum\ wind\ resistance}{\hat{u}\ for\ safe\ operation}, \tag{11}$$

where the value for the safety factor is either manually defined or subjected to safety regulation requirements. Such an approach would result in a more rigorous evaluation of hazardous indices and yield more conservative no-fly zone results.

Steps 2 and 3: defining the hazardous level and the corresponding no-fly zone using the workflow shown in Fig. 11. First, the eight possible flight directions $\boldsymbol{u}_{d,i}$ shown in Fig. 11(a) are defined for a drone at a particular location, where subscript i indicates the flight orientation. It should be noticed that considering both drone operation and wind flow in three dimensional (3D) space is complex. Therefore, since the vertical changes in drone operation are relatively minor compared to horizontal directions, the drone is assumed to operation in the drone is assumed to operate in two dimensional (2D) horizontal planes at different heights in low-altitude airspace in this step, while the urban wind flow obtained from CFD remains in 3D. This compromise provides reasonable 2D results while simplifying the computational procedure. Second, for any of the flight directions, the hazardous indices j can be evaluated in conjunction with the regional wind speed $\boldsymbol{u}_w$ using the criteria listed in Fig. 10. Third, the probability of occurrence of a specific wind direction, namely, P, is determined based on the windrose diagram shown in Fig. 1(b). This probability corresponds to a single regional wind speed and thus results in the probability of the hazardous index j, denoted as P_j. However, the same hazardous index may appear in various wind directions. Consequently, the probability of occurrence of all wind directions that result in the same hazardous index at this point is aggregated to obtain the probability $P_i(j)$ of the corresponding index under the specified flight direction. Then $P_i(j)$ represents the flight hazardous level at this point. The higher the $P_i(j)$ value, the more likely the corresponding situation will occur. Finally, for areas with high probability of deviation and unsafe, they may be considered as no-fly zone based on the safety requirements.

TABLE III. Existing delivery drones and their wind speed resistance.

Drone model	Maximum ground speed (m/s)	Wind resistance
DJI FlyCart 30[41]	20	12 m/s
Antwork TR9[42]	16.7	Level 6[a]
Smart Drone Cloud IIS[43]	16	Level 6

[a]Beaufort wind scale, level 6 corresponds to wind speeds between 10.8 and 13.8 m/s.

C. Identification of no-fly zones in Mong Kok

Given that the primary research objective of this study is to provide data support for the flight route planning of delivery drones, the wind distribution and no-fly zones during the departure and landing of drones from specific vertiports were not currently considered. In addition, the no-fly zones at heights ranging from 60 to 120 m from the ground, considering significant deviation and unsafe indices, are identified. The lower bound of 60 m is defined according to the average building height within the Mong Kok area, while the upper limit of 120 m is derived from Federal Aviation Administration (FAA) regulations in CFR PART 107,[44,45] which set the maximum flight altitude for drones at 400 feet (approximately 120 m). The ground speed of drones is set as 10 m/s. The value is lower than the maximum ground speeds listed in Table III to obtain conservative results. Finally, by combining the CFD results on urban wind distribution in low-altitude airspace and the aforementioned definitions, the probability contours of the

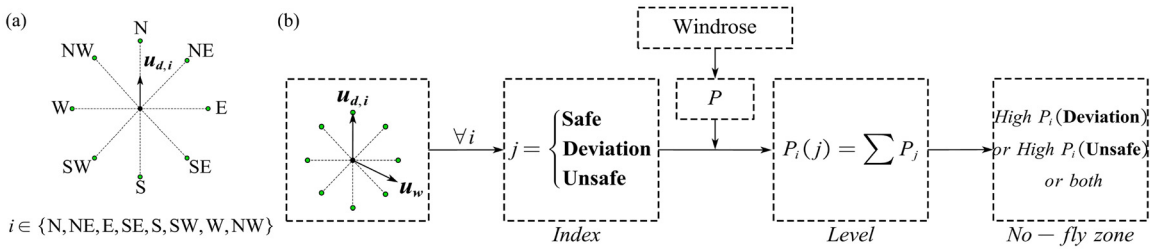

FIG. 11. Definition of hazardous level using (a) defined flight direction and (b) workflow combining hazardous indices.

flight hazardous indices at various heights in the Mong Kok area are obtained and illustrated as follows.

1. No-fly zones at different altitudes

The probability contour under two wind environments, WE1 and WE2 that listed in Table II, for a specific drone flight direction of due north and altitudes of 60, 90, and 120 m are presented in Figs. 12 and 13, respectively. A notable difference in the results between these two results is the presence of unsafe areas in WE2. This is attributed to the fact that WE1 refers to a standard wind environment, with incoming reference wind speed at 65 m being 2.5 m/s. Under this condition, the regional wind speed is relatively small according to Fig. 9, leading to the magnitude of the resultant velocity $\boldsymbol{u}_r$ do not exceed the threshold value $\hat{u}$. In contrast, WE2 represents a strong wind environment with local wind speeds up to 15 m/s, as shown in Fig. 9, resulting in a higher probability of speeds exceeding the threshold $\hat{u}$. For the same reason, overall safe areas in Fig. 13 (WE2) shrink while deviation areas increase compared with Fig. 12 (WE1), but the location is similar. Finally, the identification of no-fly zones for drone operations can be considered as areas with high probability of deviation in both WEs and unsafe areas in WE2.

In addition, the safe and deviation areas in Fig. 12 exhibit mutual exclusivity, which is due to the fact that wind speeds are generally lower in WE1, leading to the absence of unsafe conditions. Furthermore, with the altitude rising, the regional wind speeds increase, leading to reduction of areas suitable for safe operation. It can be noticed in region A in Fig. 12(b) that the probability of deviation at certain locations is high, with areas exhibiting probabilities approaching 100% for the three altitudes. The reasons for this phenomenon can be attributed to two distinct factors. First, the flow separation around blunt bodies can lead to increased local wind speed. Second, the wind speed acceleration phenomenon caused by wind crosses the narrow gaps between adjacent buildings. As a result, the resultant velocity magnitude, thus, exceeds the safety threshold, leading to high probability of deviation during drones operation. Meanwhile, the occurrence probability of safe areas at lower height, namely, 60 m, increases to 60%–70%, attributable to the smaller incoming wind velocity and the sheltering effects of the dense buildings.

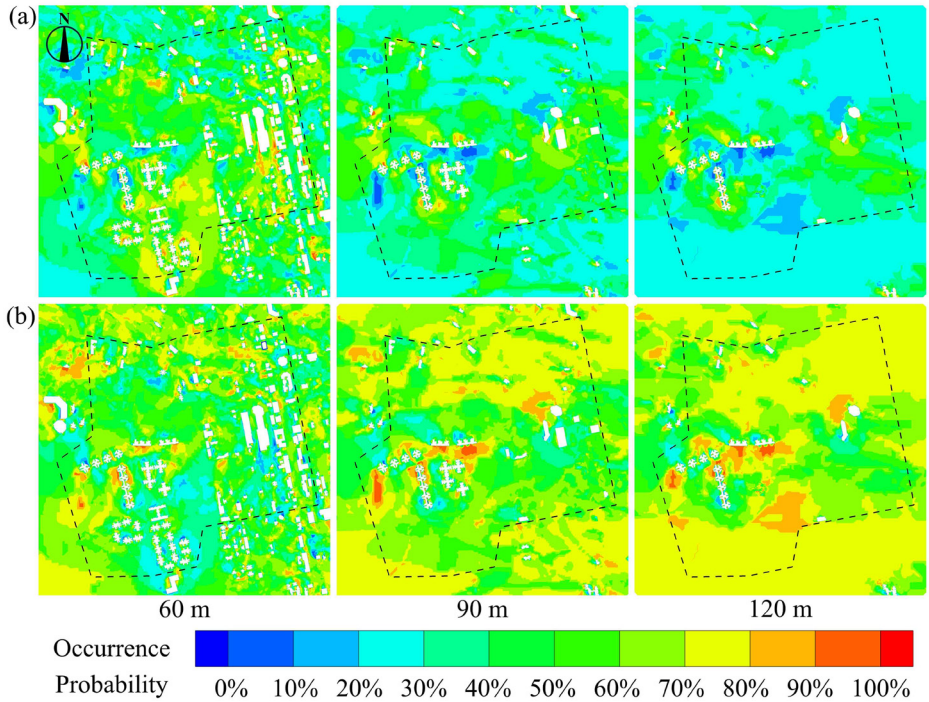

FIG. 12. Occurrence probability contours of (a) safe and (b) deviation under WE1. The dashed line indicates the boundary of the Mong Kok area.

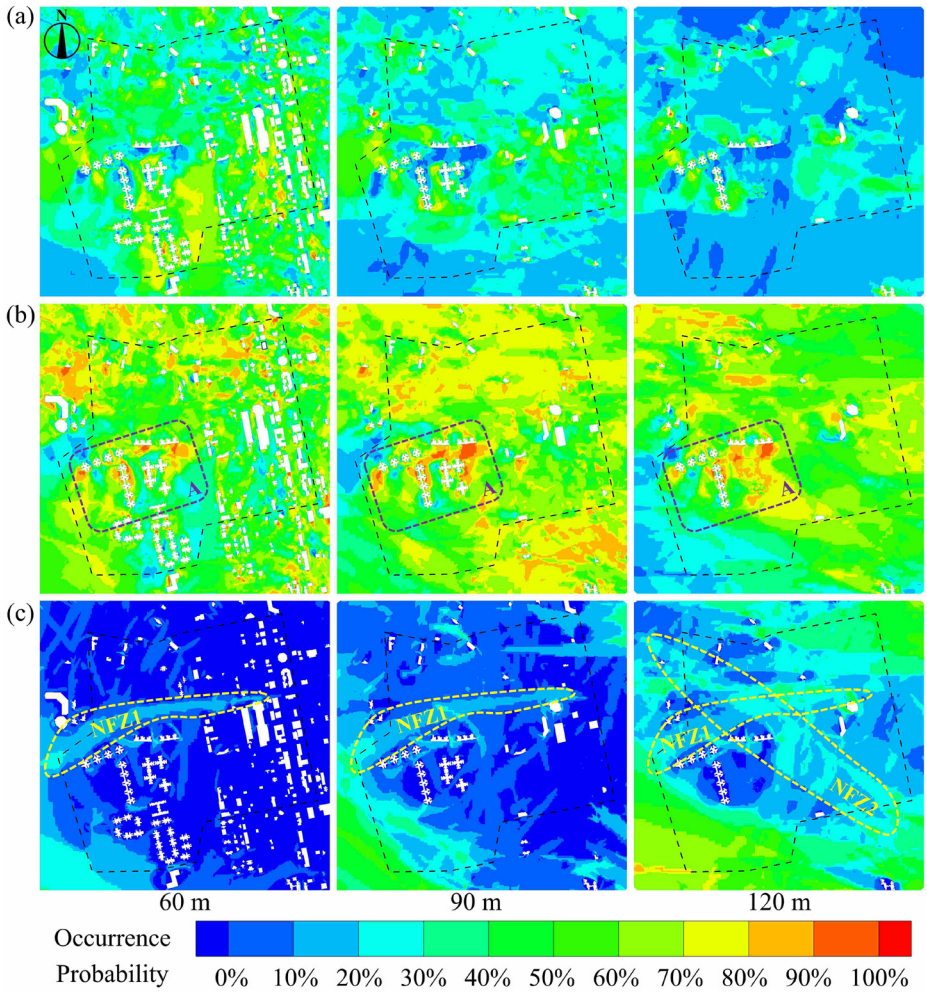

FIG. 13. Occurrence probability contours of (a) safe, (b) deviation, and (c) unsafe under WE2. The dashed line indicates the boundary of the Mong Kok area.

Furthermore, the safe areas under WE2 in Fig. 13 also reduced with the altitudes increasing due to the same reason in the WE1 case. It is worth noting that several channel-like regions emerge in the probability distribution map of unsafe areas. Specifically, at the 60 m height shown in Fig. 13(c), there is a channel consisting areas with up to 30% unsafe probability. Then this region can be considered as no-fly zone (NFZ), denoted as NFZ1. Moreover, the increased wind speeds lead to a substantial rise in the likelihood of an unsafe zone. This phenomenon is more pronounced at the 120 m level, where the extent of NFZ1 increases and another NFZ2 is observed, due to the increase in the wind speed with height combined with fewer buildings providing less obstruction. NFZ2 stretches along southeast to northwest because of the prevailing wind directions in Mong Kok concentrate from east to southeast according to the windrose data in Fig. 1(b). High probability values are also noted in the lower left position of the unsafe area maps for all three heights, resulting from the proximity of the region to the seashore and lack of building shelter.

2. No-fly zones under different flight orientations

To illustrate the results under different flight orientations of drones, the specific area from Park Avenue in Mong Kok is extracted. The probability contours of hazardous indices under WE1 are presented in Fig. 14, while those under WE2 are demonstrated in Fig. 15. The flight directions of drones are toward due north and east, respectively. A flight altitude of 110 m is chosen, as this is the altitude at which SR2 passes through the region toward north.

By comparing the safe indices shown in Figs. 14(a) and 14(b) under WE1, significant variations in the probability of safe indices near building surfaces are observed between the two flight orientations. This is due to the prevailing wind directions of Mong Kok being considered in defining the hazardous indices. As depicted in Fig. 1(b), the windrose diagram indicates that the prevailing wind direction in Mong Kok is concentrated between east and southeast. Consequently, for drones flying northward, there is a higher probability that the flight direction is not parallel to the prevailing wind direction, leading to a greater likelihood of deviation. In contrast, for drones flying eastward, the probability of a non-parallel flight direction with the prevailing wind direction is negligible, resulting in a lower likelihood of deviation. In addition, it is observed in Fig. 14(a) that SR2 passes through safe and deviation areas separately. High deviation probability areas would cause extra energy consumption for the drone to correct its flight orientation, resulting in efficiency loss. Furthermore, despite the NFZ set

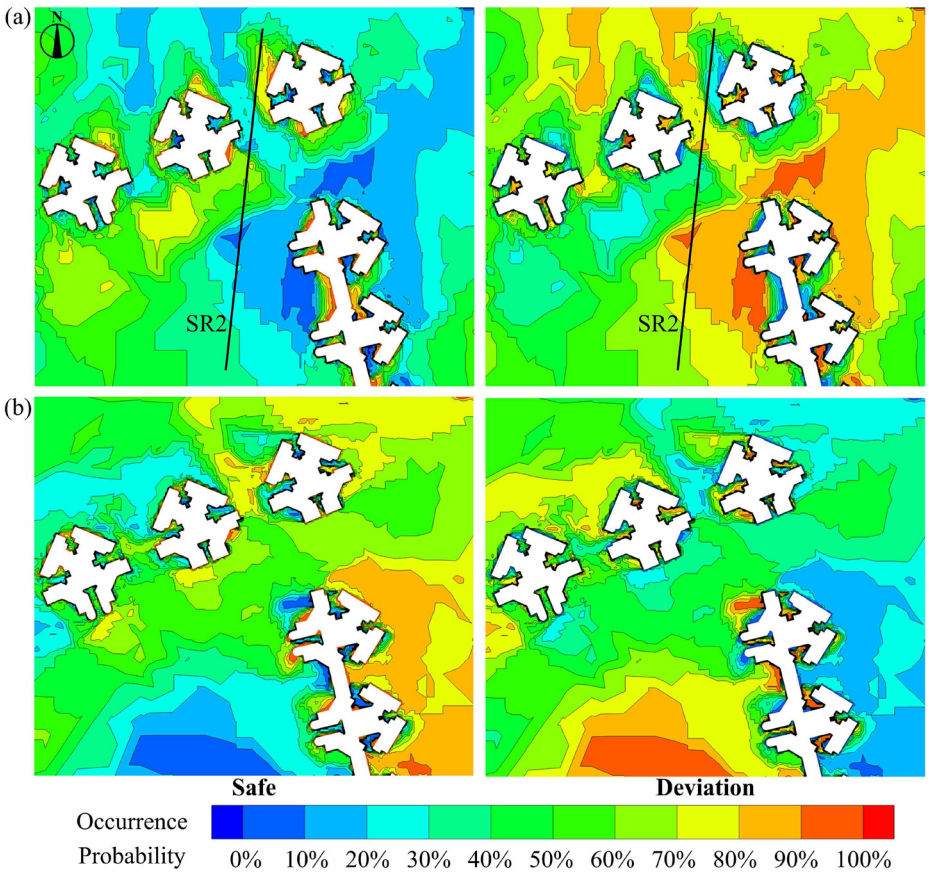

FIG. 14. Occurrence probability contour of safe and deviation under WE1 at the altitude of 110 m with fight direction toward (a) North and (b) East at Park Avenue, Mong Kok. Along with the portion of the SR2 path at 110 m altitude from South toward North.

up 10 m to 30 m from the buildings, areas beyond that range still display high possibility of deviation. This suggests that the wind environment's effects need to be considered thoroughly when planning drone flight paths in urban areas.

For the results under WE2, as illustrated in Fig. 15, a similar pattern to WE1 can be observed, but with additional unsafe zones. It is clear that when a drone navigate SR2, it can encounter safe zones, deviation zones, and even zones with an unsafe probability up to 30% simultaneously. In addition, the overall NFZ under WE2 increases compared to that under WE1, suggesting that safe flight paths under WE1 may encounter additional deviation or unsafe areas under strong wind conditions. Therefore, modification of flight paths for extreme weather conditions are needed based on the safe area map. A comprehensive examination of NFZs in varying wind environments can facilitate more optimal utilization of urban airspace and maximize the potential benefits of delivery drones, contributing to the improvement of urban air mobility management.

IV. CONCLUDING REMARKS

This study investigates the identification of no-fly zones for delivery drone operations in low-altitude airspace of a real city, in the presence of different wind environments. CFD simulation is utilized to obtain urban wind environments, which is conducted with a high-fidelity geometric and high-resolution Cartesian mesh model of the city. A two-equation RANS model, the $k-\omega$ SST model, is employed to simulate 71 cases with a range of incoming flow directions under two wind conditions (WE1 for standard and WE2 for strong wind). Focus on the effects of wind distribution in low-altitude airspace on delivery drone's flight status, the significant findings of this study are summarized as follows:

(1) The feasibility of the high-resolution computational model is validated through a grid-independence study. The wind speed distribution at two locations, MK and KP, were well fitted between two different grid schemes. Mean absolute relative errors for these locations are 0.75% and 8.8%, respectively.
(2) The analysis of wind speed distributions on two sample flight paths reveals that the wind speed varies with both height and incoming wind direction, indicating that a drone on the same path can encounter different flight states depending on the wind.
(3) A 10 m/s wind speed is chosen as a safety threshold, representing the maximum wind resistance common delivery drones can withstand with a safety factor of 1.2. This led to the formulation of three hazardous indices for drones in urban wind environments: safe, deviation, and unsafe. If the pure wind speed surpasses the threshold, the drone is deemed unsafe. If the pure wind speed stays below the threshold while the combined speed of the drone's flight velocity and wind velocity exceeds the

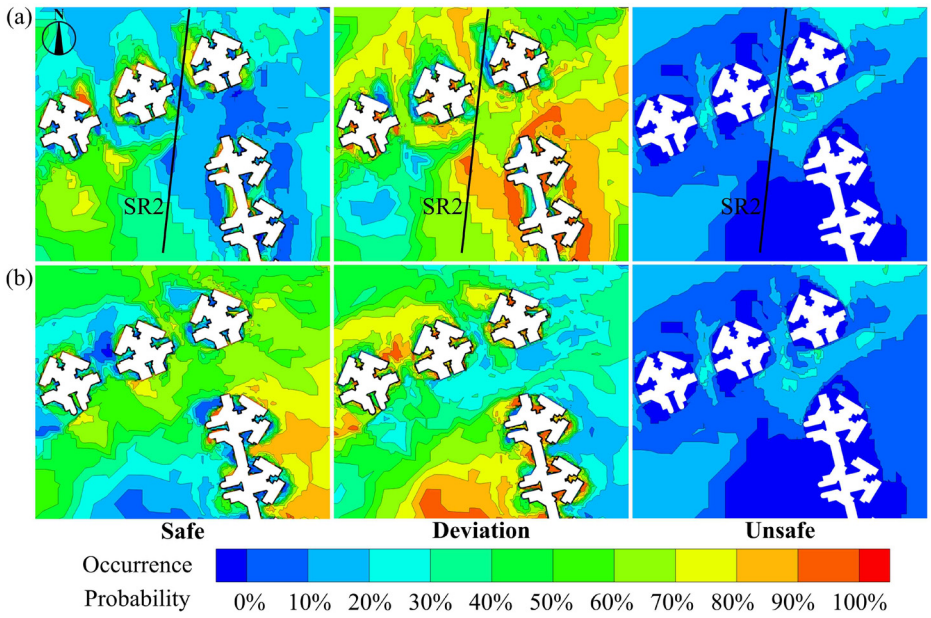

FIG. 15. Occurrence probability contour of safe, deviation, and unsafe under WE2 at an altitude of 110 m with fight direction toward (a) North and (b) East at Park Avenue, Mong Kok. Along with the portion of the SR2 path at 110 m altitude from South toward North.

threshold, drone is in deviation status. Otherwise, the drone is deemed safe.

(4) Considering various flight orientation of drones, the occurrence probabilities of the three states are calculated by combining the prevailing wind information of the real city with local wind distribution in low-altitude airspace. Based on these results, high-resolution maps at a height of 60–120 m of hazardous areas for drone operation are provided. One can utilize the presented approach to determine the hazardous area based on different speed thresholds and safety requirements.

There are limitations to this study. The RANS model used at this stage is constrained in its ability to provide time-specific results of the flow field. A viable alternative is large eddy simulation (LES), which can yield more precise flow distribution with time. Currently, the no-fly zone delineation provides results solely in two-dimensional space. In the future, a similar approach based on more accurate CFD simulations can be used to provide flight safety indicators in three-dimensional space. This will provide more assistance in demarcating the no-fly zone for delivery drones within urban environments and rationally planning their flight paths.

ACKNOWLEDGMENTS

This study was supported by City University of Hong Kong Start-up (Grant No. 9610620), Strategic Interdisciplinary Research (Grant No. 2022SIRG035), Early Career Scheme (No. CityU 21206123), General Research Fund (No. CityU 11200823), Shenzhen Basic Research Program (No. GXWD20231130143911001), GuangDong Basic and Applied Basic Research Foundation (Nos. 2023A1515111010, 2A1515240062, 2022A1515240001, and 2022A1515140136), and Shenzhen Science and Technology Program (No. KQTD20210811090112003). The authors thank Professor Jianxiang Huang from the Department of Urban Planning and Design at the University of Hong Kong for providing the 3D urban geometric model.

AUTHOR DECLARATIONS

Conflict of Interest

The authors have no conflicts to disclose.

Author Contributions

Shan Jiang: Conceptualization (equal); Data curation (equal); Formal analysis (equal); Investigation (equal); Methodology (equal); Software (equal); Validation (equal); Visualization (equal); Writing – original draft (equal); Writing – review & editing (equal). **Jinghan Wang:** Conceptualization (equal); Data curation (equal); Formal analysis (equal); Funding acquisition (equal); Investigation (equal); Methodology (equal); Software (equal); Validation (equal); Writing – review & editing (equal). **Chao Li:** Funding acquisition (equal); Resources (equal); Writing – review & editing (equal). **Jinping Ou:** Funding acquisition (equal). **Penghao Duan:** Conceptualization (equal); Funding acquisition (equal); Project administration (equal); Resources (equal); Software (equal); Supervision (equal); Writing – original draft (equal); Writing – review & editing (equal). **Lishuai Li:** Funding acquisition (equal); Resources (equal); Writing – review & editing (equal).

DATA AVAILABILITY

The data that support the findings of this study are available from the corresponding authors upon reasonable request.

REFERENCES

[1]A. Muñoz-Villamizar, J. C. Velázquez-Martínez, P. Haro, A. Ferrer, and R. Mariño, "The environmental impact of fast shipping ecommerce in inbound logistics operations: A case study in Mexico," J. Clean. Prod. **283**, 125400 (2021).

[2]S. Zhigula, K. Yurchenko, Y. Vovk, A. Oleksiuk, and L. Savchenko, "Combination of different means of parcel deliveries in urban logistics in adverse weather conditions," J. Sustainable Dev. Transp. Logistics **6**, 6–17 (2021).

[3]T. Kirschstein, "Comparison of energy demands of drone-based and ground-based parcel delivery services," Transp. Res. D: Transp. Environ. **78**, 102209 (2020).
[4]A. Raghunatha, E. Lindkvist, P. Thollander, E. Hansson, and G. Jonsson, "Critical assessment of emissions, costs, and time for last-mile goods delivery by drones versus trucks," Sci. Rep. **13**, 11814 (2023).
[5]A. Straubinger, H. L. F. de Groot, and E. T. Verhoef, "E-commerce, delivery drones and their impact on cities," Transp. Res. A: Policy Pract. **178**, 103841 (2023).
[6]T. Stathopoulos, H. Alrawashdeh, A. Al-Quraan, B. Blocken, A. Dilimulati, M. Paraschivoiu, and P. Pilay, "Urban wind energy: Some views on potential and challenges," J. Wind Eng. Ind. Aerodyn. **179**, 146–157 (2018).
[7]J. Boris, "Dust in the wind: Challenges for urban aerodynamics," AIAA Paper No. 2005-5393, 2005.
[8]H. J. S. Fernando, "Fluid dynamics of urban atmospheres in complex terrain," Annu. Rev. Fluid Mech. **42**, 365–389 (2010).
[9]P. Abichandani, D. Lobo, G. Ford, D. Bucci, and M. Kam, "Wind measurement and simulation techniques in multi-rotor small unmanned aerial vehicles," IEEE Access **8**, 54910–54927 (2020).
[10]B. H. Wang, D. B. Wang, Z. A. Ali, B. Ting, and H. Wang, "An overview of various kinds of wind effects on unmanned aerial vehicle," Meas. Control **52**, 731–739 (2019).
[11]C. A. Roseman and B. M. Argrow, "Weather hazard risk quantification for sUAS safety risk management," J. Atmos. Ocean. Technol. **37**, 1251–1268 (2020).
[12]J. D. Barton, B. Cybyk, D. G. Drewry, T. M. Frey, B. K. Funk, R. C. Hawthorne, and J. F. Keane, "Use of a high-fidelity UAS simulation for design, testing, training, and mission planning for operation in complex environments," in *Wiley Encyclopedia of Operations Research and Management Science* (John Wiley & Sons, Ltd, 2011).
[13]B. Z. Cybyk, B. E. McGrath, T. M. Frey, D. G. Drewry, J. F. Keane, and G. Patnaik, "Unsteady airflows and their impact on small unmanned air systems in urban environments," J. Aerosp. Inf. Syst. **11**, 178–194 (2014).
[14]B. Blocken, "Computational Fluid Dynamics for urban physics: Importance, scales, possibilities, limitations and ten tips and tricks towards accurate and reliable simulations," Build. Environ. **91**, 219–245 (2015).
[15]R. N. Meroney, "Ten questions concerning hybrid computational/physical model simulation of wind flow in the built environment," Build. Environ. **96**, 12–21 (2016).
[16]K. Wijesooriya, D. Mohotti, C.-K. Lee, and P. Mendis, "A technical review of computational fluid dynamics (CFD) applications on wind design of tall buildings and structures: Past, present and future," J. Build. Eng. **74**, 106828 (2023).
[17]B. Blocken, W. D. Janssen, and T. van Hooff, "CFD simulation for pedestrian wind comfort and wind safety in urban areas: General decision framework and case study for the Eindhoven University campus," Environ. Model. Software **30**, 15–34 (2012).
[18]B. Blocken and J. Persoon, "Pedestrian wind comfort around a large football stadium in an urban environment: CFD simulation, validation and application of the new Dutch wind nuisance standard," J. Wind Eng. Ind. Aerodyn. **97**, 255–270 (2009).
[19]Z. Kaseb, M. Hafezi, M. Tahbaz, and S. Delfani, "A framework for pedestrian-level wind conditions improvement in urban areas: CFD simulation and optimization," Build. Environ. **184**, 107191 (2020).
[20]J. Y. He, P. W. Chan, Q. S. Li, T. Huang, and S. H. L. Yim, "Assessment of urban wind energy resource in Hong Kong based on multi-instrument observations," Renewable Sustainable Energy Rev. **191**, 114123 (2024a).
[21]P. Jie, M. Su, N. Gao, Y. Ye, X. Kuang, J. Chen, P. Li, J. Grunewald, X. Xie, and X. Shi, "Impact of urban wind environment on urban building energy: A review of mechanisms and modeling," Build. Environ. **245**, 110947 (2023).
[22]Y. Fu, C. Y. Li, Z. Zhao, B. Zhang, K. T. Tse, C. M. Mak, Z. Chen, X. Feng, X. Lin, W. Li, and C. Lin, "Energetic and dynamic characterization of pollutant dispersion in varied building layouts through an augmented analysis procedure," Phys. Fluids **36**, 035105 (2024).
[23]W. Shan, Q. Yang, K. Guo, C. Chen, W. Zhen, and Y. C. Kim, "Across-wind response characteristics of tall-square towers in urban flow: An experimental study focused on the aeroelastic effects," Phys. Fluids **36**, 037104 (2024).
[24]J. Yu, H. Alrawashdeh, and M. Li, "Aerodynamic analysis of building with zigzag-patterned façade: Insights from large eddy simulation," Phys. Fluids **36**, 025124 (2024).
[25]M. W. Orr, S. J. Rasmussen, E. D. Karni, and W. B. Blake, "Framework for developing and evaluating MAV control algorithms in a realistic urban setting," in *Proceedings of the 2005, American Control Conference* (IEEE, 2005), pp. 4096–4101.
[26]D. Galway, J. Etele, and G. Fusina, "Modeling of urban wind field effects on unmanned rotorcraft flight," J. Aircr. **48**, 1613–1620 (2011).
[27]J. Ware and N. Roy, "An analysis of wind field estimation and exploitation_for quadrotor flight in the urban canopy layer," in *2016 IEEE International Conference on Robotics and Automation (ICRA)* (IEEE, 2016), pp. 1507–1514.
[28]C. Paz, E. Suárez, C. Gil, and C. Baker, "CFD analysis of the aerodynamic effects on the stability of the flight of a quadcopter UAV in the proximity of walls and ground," J. Wind Eng. Ind. Aerodyn. **206**, 104378 (2020).
[29]S. Jeong, K. You, and D. Seok, "Hazardous flight region prediction for a small UAV operated in an urban area using a deep neural network," Aerosp. Sci. Technol. **118**, 107060 (2021).
[30]W. Wang, "The vertical street as everyday place in the high-density city: A case study of Mong Kok, Hong Kong," Space Cult. (published online) (2023).
[31]DATA.GOV.HK, see https://data.gov.hk/en-data/dataset/hk-hko-rss-daily-mean-wind-speed for "Daily mean wind speed" (2024a).
[32]DATA.GOV.HK, see https://data.gov.hk/en-data/dataset/hk-hko-rss-daily-prevailing-wind-direction for "Daily prevailing wind direction" (2024b).
[33]Y. Yang, Z. Xie, and M. Gu, "Consistent inflow boundary conditions for modelling the neutral equilibrium atmospheric boundary layer for the SST k-w model," Wind Struct. **24**, 465–480 (2017).
[34]F. R. Menter, "Two-equation eddy-viscosity turbulence models for engineering applications," AIAA J. **32**, 1598–1605 (1994).
[35]F. Menter, M. Kuntz, and R. B. Langtry, "Ten years of industrial experience with the SST turbulence model," in *Proceedings of the 4th International Symposium on Turbulence, Heat and Mass Transfer* (Begell House Inc., West Redding, 2003), pp. 625-632.
[36]L. S. Caretto, A. D. Gosman, S. V. Patankar, and D. B. Spalding, "Two calculation procedures for steady, three-dimensional flows with recirculation," in *Proceedings of the Third International Conference on Numerical Methods in Fluid Mechanics* (Springer Berlin, Heidelberg, 1973), Vol. 19, p. 60.
[37]Y. Tominaga, A. Mochida, R. Yoshie, H. Kataoka, T. Nozu, M. Yoshikawa, and T. Shirasawa, "AIJ guidelines for practical applications of CFD to pedestrian wind environment around buildings," J. Wind Eng. Ind. Aerodyn. **96**, 1749–1761 (2008).
[38]Architectural Institute of Japan, see https://www.wind.arch.t-kougei.ac.jp/info_center/ITcontent/tamura/6.pdf for "AIJ recommendations for loads on buildings" (2004).
[39]X. He, L. Li, Y. Mo, J. Huang, and S. J. Qin, "A distributed route network planning method with congestion pricing for drone delivery services in cities," Transp. Res. C: Emerg. Technol. **160**, 104536 (2024b).
[40]Civil Aviation Department, The Government of the Hong Kong Special Administrative Region, see https://www.cad.gov.hk/documents/Safety_Requirements_Document.pdf for "Safety requirements document for small unmanned aircraft operations" (2024).
[41]DJI, see https://www.dji.com/hk-en/flycart-30/specs for "DJI - Official website" (2024).
[42]Antwork, see https://www.antwork.link/index.html for "Innovator of urban drone delivery" (2024).
[43]ML Smart Drone UAV, see https://www.smd-uav.com/product/cloud-iis/ for "CLOUD IIS" (2023).
[44]P. Kopardekar, J. Rios, T. Prevot, M. Johnson, J. Jung, and J. E. Robinson, "Unmanned aircraft system traffic management (UTM) concept of operations," AIAA Paper No. AIAA 2016-3292, 2016.
[45]Y. Wu, K. H. Low, B. Pang, and Q. Tan, "Swarm-based 4D path planning for drone operations in urban environments," IEEE Trans. Veh. Technol. **70**, 7464–7479 (2021).